

Explaining the GeV antiproton/ γ -ray excesses and W-boson mass anomaly in an inert two Higgs doublet model

Cheng-Rui Zhu^{1,2}, Ming-Yang Cui^{1*}, Zi-Qing Xia¹, Zhao-Huan Yu³, Xiaoyuan Huang^{1,4*}, Qiang Yuan^{1,4*}, Yi-Zhong Fan^{1,4*}

¹Key Laboratory of Dark Matter and Space Astronomy,

Purple Mountain Observatory, Chinese Academy of Sciences, Nanjing 210023, China

²Shandong Institute of Advanced Technology, Jinan 250100, China

³School of Physics, Sun Yat-Sen University, Guangzhou 510275, China

⁴School of Astronomy and Space Science, University of Science and Technology of China, Hefei 230026, Anhui, China *

For the newly discovered W -boson mass anomaly, one of the simplest dark matter (DM) models that can account for the anomaly without violating other astrophysical/experimental constraints is the inert two Higgs doublet model, in which the DM mass (m_S) is found to be within $\sim 54 - 74$ GeV. In this model, the annihilation of DM via $SS \rightarrow b\bar{b}$ and $SS \rightarrow WW^*$ would produce antiprotons and gamma rays, and may account for the excesses identified previously in both particles. Motivated by this, we re-analyze the AMS-02 antiproton and Fermi-LAT Galactic center gamma-ray data. For the antiproton analysis, the novel treatment is the inclusion of the charge-sign-dependent three-dimensional solar modulation model as constrained by the time-dependent proton data. We find that the excess of antiprotons is more distinct than previous results based on the force-field solar modulation model. The interpretation of this excess as the annihilation of $SS \rightarrow WW^*$ ($SS \rightarrow b\bar{b}$) requires a DM mass of $\sim 40 - 80$ ($40 - 60$) GeV and a velocity-averaged cross section of $O(10^{-26}) \text{ cm}^3 \text{ s}^{-1}$. As for the γ -ray data analysis, besides adopting the widely-used spatial template fitting, we employ an orthogonal approach with a data-driven spectral template analysis. The fitting to the GeV γ -ray excess yields DM model parameters overlapped with those to fit the antiproton excess via the WW^* channel. The consistency of the DM particle properties required to account for the W -boson mass anomaly, the GeV antiproton excess, and the GeV γ -ray excess suggest a common origin of them.

I. INTRODUCTION

The dark matter (DM) problem remains one of the biggest mysteries of the cosmos. Among many kinds of candidates, the weakly interacting massive particle (WIMP) is the most naturally motivated by the thermal production in the early Universe and its proper relic density today [1]. Quite a lot of efforts have been spent in looking for WIMP DM in various kinds of experiments. No convincing signal has been identified in the direct detection experiments and very stringent constraints on the WIMP-nucleon interaction strength have been set (e.g., [2, 3]). As for the indirect detection aiming to identify the products of the annihilation or decay of the DM particles [1, 4], some anomalies have been claimed in the past decade, such as the positron and electron excesses [5–7], the antiproton excess¹ [10, 11], and the Galactic center γ -ray excess (GCE; [12–15]). While the positron and electron excesses might be naturally explained by astrophysical pulsars [16, 17] and the DM interpretation is severely constrained by γ -ray and cosmic microwave background observations [18], the antiproton excess and the GCE which point to a consistent DM interpretation survive other constraints [19–21]. In spite that uncertainties of various astrophysical and particle physics ingredients exist [22–32], common implications on the DM scenario from multi-messengers are very interesting. In any case, additional tests of this scenario from independent probes are very important in finally detecting DM particles.

Very recently, the measured W -boson mass by the CDF collaboration shows $\sim 7\sigma$ deviation from the prediction of the standard model (SM), which strongly suggests the existence of new physics beyond the SM [33]. One of the most economic solutions is to introduce an additional scalar doublet, in which the non-SM scalars can enhance the W -boson mass via the loop corrections. With a proper discrete symmetry \mathbb{Z}_2 , the lightest new scalar in the doublet can be stable and play the role of DM. One realization of this mechanism is the inert two Higgs doublet model (i2HDM), which is shown to be able to accommodate the new W -boson mass and various astrophysical/experimental constraints simultaneously [34]. Considering available constraints from the collider searches for new physics, the electroweak precision tests, the direct detection of DM, and the relic density of DM, the mass of DM is limited within the range of $54 \text{ GeV} < m_S < 74 \text{ GeV}$, and the annihilation is dominated by the process of $SS \rightarrow WW^*$ for $m_S \geq 62 \text{ GeV}$ and by $SS \rightarrow b\bar{b}$ otherwise.

It is thus essential to examine whether the astrophysical data are in support of such an attractive possibility or not. For such a purpose, we re-analyze the AMS-02 antiproton and Fermi-LAT Galactic center γ -ray data. Compared with previous works, we improve the technical treatments in several aspects to reduce potential uncertainties of the analyses. For the antiproton modeling, our novel treatment is to include the charge-sign-dependent three-dimensional (3D) solar modulation model [35, 36] as constrained by the time-dependent AMS-02 proton data [37]. To investigate the GCE, taking a data-driven method, we identify the background components for the γ -ray sky solely with their spectral properties as in Ref. [38], called as the spectral template analysis. The traditional spatial template analysis will also be employed for a cross check. To minimize the possible contamination from

* mycui@pmo.ac.cn (MYC); xyhuang@pmo.ac.cn (XH);
yuanq@pmo.ac.cn (QY); yzf@pmo.ac.cn (YZF)

¹ See also Refs. [8, 9] for possible hints of excess from measurements prior to AMS-02.

the astrophysical contribution in the galactic bulge [28, 29], a large portion of the galactic disk is masked. We find consistent DM particle properties to account for the W -boson mass anomaly, the GCE, and the antiproton excess, which are in favor of a common origin.

II. ANTIPROTONS

In previous studies, the solar modulation of the antiprotons is usually assumed to be the same as that of protons and the force-field approximation [39] was often adopted². However, it is known that the particles with opposite charge have very different trajectories in the heliosphere (e.g., [41]). Such an effect should be taken into account to properly reproduce the local interstellar spectra (LIS) of protons and antiprotons. For such a purpose, here we employ the charge-sign-dependent 3D solar modulation model developed in [42, 43]. The transportation of charged particles inside the heliosphere is described by the Parker's equation [44]

$$\frac{\partial f}{\partial t} = -(\mathbf{V}_{\text{sw}} + \langle \mathbf{v}_d \rangle) \cdot \nabla f + \nabla \cdot (\mathbf{K}^{(s)} \cdot \nabla f) + \frac{1}{3} (\nabla \cdot \mathbf{V}_{\text{sw}}) \frac{\partial f}{\partial \ln p}, \quad (1)$$

where $f(\mathbf{r}, p, t)$ is the phase space distribution function of cosmic rays, \mathbf{V}_{sw} is the solar wind speed, $\langle \mathbf{v}_d \rangle$ is the pitch-angle-averaged drift velocity, $\mathbf{K}^{(s)}$ is the symmetric diffusion tensor, and p is the momentum of the particle. See the Appendix Sec. A for more details. We solve the Parker's equation numerically employing the stochastic differential equations [42, 43].

The LIS of protons is derived through fitting to the Voyager-1 [45], AMS-02 [6], and DAMPE [46] data. To do this fitting, we employ the GALPROP³ code to calculate the propagation of cosmic rays in the Milky Way [47]. The detailed fitting procedure is described in the Appendix Sec. B. The antiproton LIS, calculated based on the proton LIS, is shown by the black solid line in Fig. 1. Here we use the new parameterization of the antiproton production cross section from Ref. [48] and an energy-dependent nuclear enhancement factor to take into account the contribution from heavy nuclei in both cosmic rays and the interstellar medium [49].

We fit the time-dependent proton fluxes measured by AMS-02 [37] to obtain the solar modulation parameters. The AMS-02 monthly proton fluxes are grouped into 9 time bins, each contains 6 Bartels rotations, from May 19, 2011 to May 26, 2015, corresponding to the antiproton measurement time [50]. The fitting results of the main modulation parameters are given in the Appendix Sec. C. Using the best-fit parameters, we calculate the modulated antiproton spectrum, as shown by the blue dashed line in Fig. 1. We find that, the

modulated background spectrum from the cosmic ray interactions is lower than the data between 1 and 30 GeV, consistent with previous studies [10, 11, 19]. Intriguingly, the difference between the antiproton data and the predicted astrophysical background is more distinct than that found previously with the force-field solar modulation. This is perhaps due to that particles with negative charge were modulated more severely than positive charged particles after the reversal of the heliospheric magnetic field [51].

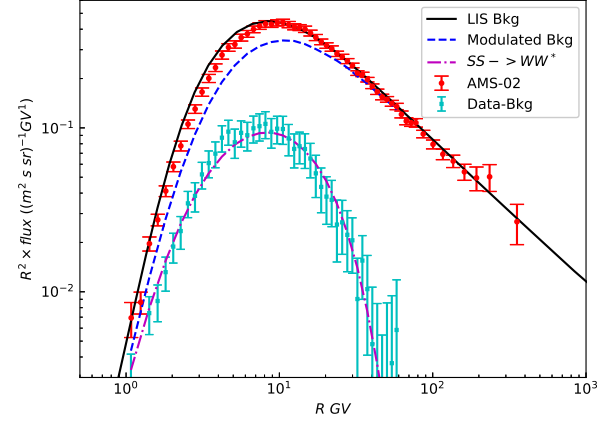


FIG. 1. The LIS (solid) and the modulated (dashed) spectra of background antiprotons, compared with the data [50]. The cyan points denote the AMS-02 data minus the modulated background results, and the dash-dotted line shows the antiproton spectrum from DM annihilation into WW^* with $(m_S, \langle \sigma v \rangle) = (62.6 \text{ GeV}, 1.5 \times 10^{-26} \text{ cm}^3 \text{ s}^{-1})$.

Then we consider the DM contribution to the antiprotons. The DM density distribution is assumed to be a generalized Navarro-Frenk-White profile [52], with a local density of 0.4 GeV cm^{-3} and an inner slope of 1.28^4 . The annihilation into $b\bar{b}$ or W^+W^- is considered. For DM mass $m_S < m_W$, we also consider the off-shell annihilation into WW^* , as in the case of i2HDM. The DM annihilation into WW^* is simulated with MadGraph5_aMC@NLO [55], including all three-body final states of one on-shell and one off-shell W bosons. We further utilize PYTHIA 8 [56] to carry out the simulation of final state radiation, hadronization, and particle decays, and obtain the corresponding energy spectra of antiprotons and γ rays.

We perform a likelihood fitting to the antiproton data, with a marginalization of the constant re-scaling factor of the background, and obtain the constraints on the $(m_S, \langle \sigma v \rangle)$ parameters. The results are shown in Fig. 2 for the WW^* channel, and the results for the $b\bar{b}$ channel are shown in the Appendix Sec. G. The favored mass of DM particles is from 40 to 60 GeV for the $b\bar{b}$ channel, and from 40 to 80 GeV for the WW^* channel, respectively, and the annihilation cross

² An empirical approach to derive a time, rigidity, and charge-sign dependent force-field modulation potential has been developed in Ref. [40].

³ <https://galprop.stanford.edu/>

⁴ This density profile is consistent with the prediction from the cold DM model, which is largely consistent with observations of DM dominated systems, such as Ultra Faint Dwarf galaxies [53, 54].

section is around the level of the thermal production of DM, i.e., $O(10^{-26} \text{ cm}^3 \text{ s}^{-1})$. We also consider the influence of uncertainties of solar modulation on the likelihood fitting. The result is shown in the Appendix Sec. D. We can see that the contours of WW^* overlap well with the i2HDM model parameters to fit the m_W anomaly [34]. Two possible regions of the i2HDM parameter space with DM mass of about 70 – 73 GeV (for four-point interactions) and about 62 – 63 GeV (for the Higgs resonance and scalar-pseudoscalar co-annihilation region) can commonly account for the antiproton excess and the m_W anomaly. In the even lower-mass window ($m_S < 62$ GeV), the i2HDM model to fit the m_W anomaly typically requires DM to annihilate dominantly into $b\bar{b}$ but with a much smaller cross section and seems not able to produce enough antiprotons.

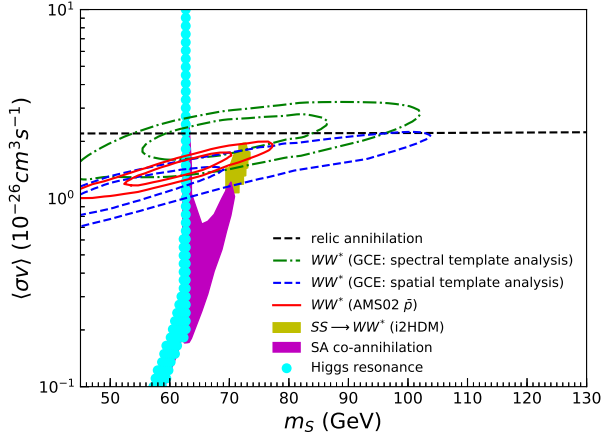


FIG. 2. The favored DM parameter space via fitting to the antiproton and GCE data (1σ and 2σ from inside to outside) for the WW^* channel, as well as the i2HDM model parameters to fit the W -boson mass anomaly (the 95% region, adopted from Ref. [34]). The black dashed line is the mass-dependent relic annihilation cross section [57].

III. GALACTIC CENTER GAMMA RAYS

The Galactic center is expected to gather high densities of DM, which makes it appealing for the indirect detection of DM. A spatially extended excess of γ rays in the 1–10 GeV energy range, with respect to the expected emission of cataloged point sources and astrophysical diffuse components, was found in the Fermi-LAT observations (e.g., [12–15]), named as the GCE.

To investigate this GeV excess, Refs. [38, 58–60] adopt the spectral template analysis, which attempts to reduce the influences from uncertainty in spatial templates of astrophysical diffuse components. The γ -ray sky is decomposed into point sources and diffuse emission component by D³PO and spectra from the “cloud-like” component and the “bubble-like” component, for diffuse emission from hadronic and leptonic processes, were derived from two distinctive regions [58]. The

astrophysical background is investigated by including point sources and data-driven spectral templates. Further, the spectral information of DM annihilation is used as a new component. The existence of the GCE was confirmed and consistent DM parameters were derived in this alternative way if the spatial distribution of the GCE is fixed as in Ref. [15], although an indication of a spatial correlation between the GCE and astrophysical component was shown if the spatial distribution of the GCE is free [38]. Note that following Ref. [38], we also consider the isotropic component in the spectral template analysis. Though this component is sub-dominant in the Galactic center region, it would be important in the region far away from the galactic disk. See more details of the spectral template analysis in Ref. [38].

Besides the annihilation channel of $SS \rightarrow b\bar{b}$ [38], here we apply this method to investigate whether the annihilation of DM via $SS \rightarrow WW^*$ could be consistent with the Galactic center γ -ray data. The γ -ray dataset, the point sources, and the spectra from the “cloud-like” component, the “bubble-like” component and the isotropic γ -ray component are the same as in Ref. [38]. Here the DM density distribution is the same as that for the antiproton analysis in Sec. II. The region of interest (ROI) used in this analysis is a square region selected by Galactic latitudes $|b| < 20^\circ$ and Galactic longitudes $|l| < 20^\circ$, with a mask of the Galactic plane with $|b| < 8^\circ$, to eliminate the influence from the boxy bulge, the nuclear bulge and the X-shaped bulge [28, 29].

We scan the DM parameters to calculate the likelihood map of different parameters. See the Sec. E of the Appendix for the selected ROI and likelihood map of the GCE fitting. The best fit DM parameters we got are $(m_S, \langle\sigma v\rangle) = (68.5 \text{ GeV}, 2.1 \times 10^{-26} \text{ cm}^3 \text{ s}^{-1})$ for the WW^* channel, and $(77.5 \text{ GeV}, 1.7 \times 10^{-26} \text{ cm}^3 \text{ s}^{-1})$ for the $b\bar{b}$ channel. The 1σ and 2σ contours of the fittings (WW^*) are given in Fig. 2 by green dash-dotted lines. At 2σ level, the favored region of the WW^* channel from the GCE, the antiproton excess, and the m_W anomaly overlap with each other. Given that there should be additional uncertainties from various aspects of the theoretical modeling (e.g., the density profile of DM in the inner Galaxy and the simulation of the spectra of the annihilation final state particles), we regard these three anomalies are accounted for simultaneously with the same DM model component. The results for the $b\bar{b}$ channel are shown in the Appendix Sec. G.

As a complementary check, we also take the traditional spatial template regression techniques [13, 15, 32] to fit the Fermi-LAT γ -ray observations to investigate the GCE. See the Appendix Sec. F for more details of the spatial template analysis. Corresponding to the minimums of mean χ^2 values, the best fit DM parameters $(m_S, \langle\sigma v\rangle)$ we obtained are $(49.7 \text{ GeV}, 1.0 \times 10^{-26} \text{ cm}^3 \text{ s}^{-1})$ for the WW^* channel and $(50.1 \text{ GeV}, 6.7 \times 10^{-27} \text{ cm}^3 \text{ s}^{-1})$ for the $b\bar{b}$ channel, respectively. The 1σ and 2σ contours (WW^*) for this spatial template analysis are shown in Fig. 2 as blue dashed lines. Same as the result of the previous spectral template analysis, we also find the 2σ confidence region of the WW^* channel from the GCE, the antiproton excess and the m_W anomaly invariably overlap with each other.

IV. CONCLUSION AND DISCUSSION

Very recently, the CDF collaboration reported a statistically significant W -boson mass excess [33], which strongly indicates the new physics beyond the SM [61, 62]. One interesting possible solution is the i2HDM, which indicates dark matter particles with a mass of $\sim 50 - 70$ GeV, and with the cross section $\sim O(10^{-26} \text{ cm}^3 \text{ s}^{-1})$ for the $SS \rightarrow WW^*$ annihilation channel. If correct it might yield observable gamma-rays and anti-protons in the Galaxy. Motivated by such a possibility, in this work we re-analyze the Fermi-LAT gamma-ray and AMS-02 anti-proton data and then investigate the possible DM origin of the identified excesses. While our excess signals are generally in agreement with previous works, we incorporate several new technical treatments in the analysis such as the charge-sign-dependent 3D solar modulation of anti-protons and a spectral template fitting scheme of γ rays, as well as the off-shell annihilation channel of $SS \rightarrow WW^*$. It is very intriguing to find that the three very different anomalies can be simultaneously accounted for in a minimal DM model with DM particle mass of $\sim 60 - 70$ GeV. The velocity-weighted annihilation cross section is about $\langle \sigma v \rangle \sim O(10^{-26} \text{ cm}^3 \text{ s}^{-1})$ and is just consistent with the expectation of the thermal production of DM. The required DM parameters are also consistent with constraints from other probes such as neutrinos [63]. Although there are various kinds of uncertainties of the antiproton background calculation like the propagation model of cosmic rays, the hadronic interaction models, and/or the solar modulation which is partially addressed in this work [22–25], as well as debates of the astrophysical or DM origin of the GCE [26–32], the DM interpretation of the three independent signals seems to be a straightforward, economic, and attractive possibility. The ongoing direct detection experiments such as the PandaX-4T, Xenon-nT and LUX has a good prospect to detect it in the near future, as shown in [34].

We comment that the antiproton excess identified in 1 – 40 GeV (Fig. 1) is likely hard to be accounted for by astrophysical sources. As a commonly proposed scenario that secondary particles may also be produced via interactions around the accelerating sources (e.g., supernova explosion in molecular clouds), harder spectra of secondary particles are expected which should be more evident at high energies [64, 65]. If we artificially attribute the identified low-energy antiproton excess to an astrophysical secondary particle component, the corresponding B/C ratio would be significantly higher than the measurements, as shown in the Supplemental Material of Ref. [10].

ACKNOWLEDGMENTS

This work is supported by the National Key R&D program of China (No. 2021YFA0718404), the National Natural Science Foundation of China (No. 11921003, 11903084, 12003069, 12220101003), Chinese Academy of Sciences (CAS), the CAS Project for Young Scientists in Basic Research (No. YSBR-061), and the Program for Innovative Tal-

ents and Entrepreneur in Jiangsu.

APPENDIX

A. Setup of the 3D modulation model

We describe in more detail the ingredients of the 3D modulation model. The diffusion tensor, $\mathbf{K}^{(s)}$, given in the heliospheric magnetic field (HMF) aligned coordinates, is

$$\mathbf{K}^{(s)} = \begin{pmatrix} \kappa_{\parallel} & 0 & 0 \\ 0 & \kappa_{\perp\theta} & 0 \\ 0 & 0 & \kappa_{\perp r} \end{pmatrix}, \quad (2)$$

where κ_{\parallel} is the parallel diffusion coefficient, $\kappa_{\perp r}$ and $\kappa_{\perp\theta}$ are the two perpendicular diffusion coefficients in the radial and latitudinal directions. In our work, we parameterize the parallel diffusion coefficient as [35, 66]

$$\kappa_{\parallel} = \kappa_{\parallel}^0 \beta \frac{B_0}{B} \left(\frac{p}{p_0} \right)^{\alpha_1} \left[\frac{\left(\frac{p}{p_0} \right)^s + \left(\frac{p_k}{p_0} \right)^s}{1 + \left(\frac{p_k}{p_0} \right)^s} \right]^{\frac{\alpha_2 - \alpha_1}{s}}, \quad (3)$$

where β is the particle speed in unit of the speed of light, B is the magnitude of the HMF with $B_0 = 1$ nT, p is the particle momentum, $p_0 = 1$ GV, and s is the smoothness transition parameter which is fixed to be 2.2. The perpendicular diffusion coefficients are assumed to be $\kappa_{\perp r, \perp\theta} = 0.02\kappa_{\parallel}$. The free parameters of the diffusion coefficient are κ_{\parallel}^0 , α_1 , α_2 , and p_k .

We adopt the standard Parker HMF model [67] as

$$\mathbf{B}(r, \theta) = \frac{A_0 B_{\oplus}}{r^2} \left(\mathbf{e}_r - \frac{r\Omega \sin \theta}{V_{\text{sw}}} \mathbf{e}_{\theta} \right) [1 - 2H(\theta - \theta_{\text{cs}})], \quad (4)$$

where B_{\oplus} is the reference value at the Earth's location, $A_0 = A \sqrt{1 + \Omega^2/V_{\text{sw}}^2}$ with $A = \pm 1$ describing the polarity of the HMF, Ω is the angular velocity of the Sun, $H(\theta - \theta_{\text{cs}})$ is the Heaviside function and θ_{cs} determines the polar extent of the Heliospheric Current Sheet (HCS). Following Ref. [68], we have

$$\cot(\theta_{\text{cs}}) = -\tan(\alpha) \sin(\phi^*), \quad (5)$$

where α is the HCS tilt angle, $\phi^* = \phi + r\Omega/V_{\text{sw}}$ is the foot point at the Sun for the corresponding spiral magnetic field line with ϕ being the longitude angle of the current sheet surface.

The drift velocity $\langle \mathbf{v}_d \rangle$ can be described as [69, 70]

$$\langle \mathbf{v}_d \rangle = \frac{p\nu}{3qB} \nabla \times \frac{\mathbf{B}}{B}, \quad (6)$$

where q is the particle's charge and ν is the velocity. To avoid the singularity of the drift close to the HCS where the direction of the magnetic field changes abruptly, the drift velocity within $(-2R_g, 2R_g)$ to the HCS is approximated as $\nu/6$ in magnitude and the direction is along the HCS [66, 70]. Here R_g is the gyro radius of the particle. As discussed in Ref. [71], the drift velocity may be suppressed, especially for when the solar activity is strong. Here we multiply a factor $K_d \in [0, 1]$ on the drift velocity and fit K_d with the data.

B. The proton LIS

The Voyager-1 measurements of proton fluxes outside the heliosphere [45] and the AMS-02 measurements at high energies (e.g., $\gtrsim 50$ GeV) [6] can robustly constrain the low- and high-energy parts of the proton LIS. However, for the intermediate energy range, the LIS entangles with the solar modulation, and thus a model-dependence is unavoidable. The antiproton LIS depends further on the distribution and interactions of protons in the Milky Way as well as the interstellar propagation of particles. The GALPROP code is used to calculate the propagation of cosmic rays. The propagation parameters were derived through fitting the secondary and primary nuclei of cosmic rays [72]. The reacceleration model is adopted as the benchmark of this work since it fits the secondary nuclei data much better than the model without reacceleration. We use a cubic spline method [73] to describe the source spectrum of protons, and employ the force-field modulation model to approximate the average solar modulation of protons during the data-taking period of AMS-02 [6]. The solid line in Fig. A1 shows the calculated LIS of protons using the best-fit source parameters. Also shown are AMS-02 proton data from [74] with the data-taking period is covered by the monthly AMS-02 proton data, and the 3D modulation (dash-dotted) with parameters derived in this work (see below). The differences between the 3D modulated spectrum and data is very small.

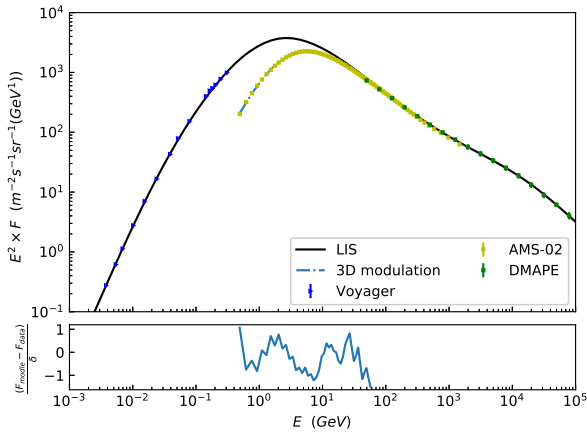


FIG. A1. The LIS (solid) and modulated (dash-dotted for the 3D modulation) spectrum of protons, compared with the Voyager-1 [45], AMS-02 [74], and DAMPE [46] data. The lower sub-panel shows the residuals for 3D modulation.

C. Fit to the time-dependent proton fluxes

The monthly proton fluxes reported in [37] are used to derive the time-dependent solar modulation parameters. To reduce the computation load, the monthly data are rebinned into nine time bins with Bartels rotations: 2426 – 2431, 2432 –

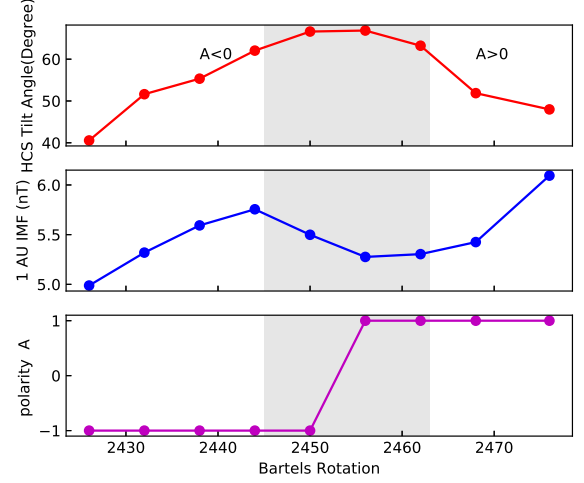


FIG. A2. Top: the HCS tilt angle from the WSO. Middle: the average HMF values from the ACE. Bottom: the polarity of the HMF adopted in this work. The gray belts denote the period when the polarity is uncertain [75].

2437, 2438 – 2443, 2444 – 2449, 2450 – 2455, 2456 – 2461, 2462 – 2467, 2468 – 2475, and 2476 – 2479, which cover the time interval of the antiproton measurements [50]. Note that there is no data during Bartels rotations 2472 – 2473. Since there is about one year time lag between the cosmic ray flux modulation and solar activities [73], following Ref. [36], we utilize the previous 13 month averaged interplanetary parameters for every month, including the HCS tilt angle from the Wilcox Solar Observatory (WSO⁵), the average HMF values from the Advanced Composition Explorer (ACE⁶). As the time bin we use here is about half a year, we further take the six month mean values of the interplanetary parameters. As for the polarity, we assume $A < 0$ before Bartels rotation 2455, and $A > 0$ after then. The finally used interplanetary parameters are shown in Fig. A2

⁵ <http://wso.stanford.edu>

⁶ <http://www.srl.caltech.edu/ACE/ASC/index.html>

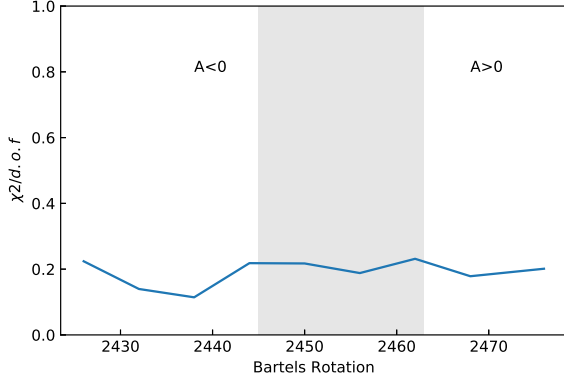


FIG. A3. The reduced χ^2 for the fittings of the time-dependent proton fluxes. The period with uncertain HMF polarity is marked in gray.

The reduce χ^2 of the fittings is show in Fig. A3, and the best-fit parameters of κ_{\parallel}^0 , α_1 , α_2 , p_k , and K_d are shown in Fig. A4. We can see that all the parameters correlate with the polarity reversal of the HMF, indicating the importance of considering the time-dependent modulation effect in detail rather than an average modulation effect. The diffusion coefficient κ_{\parallel}^0 is inversely correlated with the solar activities. This is understandable, since more turbulent of the interplanetary environment means a slower diffusion. The drift suppression factor K_d is larger for $A < 0$, and smaller for $A > 0$, consistent with previous work [76, 77]. Our fittings further show that probably no break of the diffusion coefficient is required when $A < 0$, given the very close values of α_1 and α_2 .

D. Impact of uncertainties of the solar modulation fitting

To quantify the uncertainties of the solar modulation fitting, we adopt the modulation parameters which match the upper and lower boundaries of the proton data and repeat the likelihood fitting of the DM contribution to antiprotons. The resulting 1σ and 2σ constraints on the $(m_S, \langle\sigma v\rangle)$ parameters are shown in Fig. A5. This results in uncertainties of $\sim 20\%$, mainly on the annihilation cross section.

E. The ROI, the likelihood map and another spectral component of the GCE spectral template fitting

The left panel of Fig. A6 shows the ROI of our analysis. The middle and right panels show the likelihood maps, characterized by $\Delta\chi^2 = \chi^2 - \chi_{\min}^2$ ⁷, on the $(m_S, \langle\sigma v\rangle)$ parameter plane for the $SS \rightarrow WW^*$ channel.

F. The GCE spatial template analysis

For the spatial template analysis, we adopt a similar method as in previous work [13, 15, 32]. We use Fermi Pass 8 data, version P8R3 and class ULTRACLEANVETO, recorded from Aug 4 2008 to Feb 1 2020, in total 600 weeks. To suppress the contamination from γ -ray generated by CR interactions in the upper atmosphere, photons collected at zenith angles larger than 90° are removed. Moreover, we adopt the specifications (DATA_QUAL>0) &&(LAT_CONFIG==1) to select the good quality data. We use the healpix projection [78] for the spatial binning of data, with the resolution parameter nside = 256. And we also bin the data, from 600 MeV to 300 GeV, into 15 logarithmically distributed energy bins. We use the Fermitools version 1.2.1 to calculate the relevant exposure-cube files and exposure maps, with the instrumental response function P8R3_ULTRACLEANVETO_V2.

The likelihood for estimating the contribution from different components is constructed as

$$-2 \ln \mathcal{L} = 2 \sum_{i,j} (\mu_{i,j} - k_{i,j} \ln \mu_{i,j}) + \chi_{\text{ext}}^2, \quad (7)$$

where $\mu_{i,j}$ and $k_{i,j}$ are the expected and observed number of photons in the energy bin i and the pixel j , respectively, and χ_{ext}^2 is used to further constrain the contribution from some model components. For the expected number of photons, we take

$$\begin{aligned} \mu_{i,j} = & q_i^{\pi^0+\text{brems}} N_{i,j}^{\pi^0+\text{brems}} + q_i^{\text{ics}} N_{i,j}^{\text{ics}} + q_i^{\text{iso}} N_{i,j}^{\text{iso}} \\ & + q_i^{\text{bubble}} N_{i,j}^{\text{bubble}} + q_i^{\text{psc}} N_{i,j}^{\text{psc}} \\ & + q_i^{\text{gNFW}} N_{i,j}^{\text{gNFW}} + q_i^{\overline{\text{gNFW}}} \overline{N_{i,j}^{\text{gNFW}}}, \end{aligned} \quad (8)$$

where $N_{i,j}^{\pi^0+\text{brems}}$, $N_{i,j}^{\text{ics}}$, $N_{i,j}^{\text{iso}}$, $N_{i,j}^{\text{bubble}}$, $N_{i,j}^{\text{psc}}$, $N_{i,j}^{\text{gNFW}}$, and $\overline{N_{i,j}^{\text{gNFW}}}$ are predicted number of photons for the galactic diffuse π^0 decay emissions plus the bremsstrahlung emissions, the inverse Compton scattering emissions, the isotropic γ -ray emissions, the Fermi Bubbles, point sources, the GCE in the region defined in the left panel of Fig. A6, and the "GCE-like" component in the complement of the above mentioned region, respectively. And q_i stands for the scaling factor for each component in each energy bin. For the galactic diffuse emissions, we use 128 templates introduced in Ref. [79], and we tie the π^0 decay emissions and the bremsstrahlung emissions into a single component since morphologies of these two emissions are both primarily determined by the interstellar medium gas [15, 32]. For the isotropic γ -ray emissions, we use a flat and homogeneous flux to take into account the combined emission from unresolved point sources and misidentified cosmic rays. For the Fermi Bubbles, we adopt the spatial template from Ref. [80]. For point sources, the predicted photon counts are calculated by *gmodel* for all detected sources in the 4FGL catalog [81, 82]. For the GCE in the interested region, we take the same generalized Navarro-Frenk-White profile as in the antiproton and spectral template analysis. And for the "GCE-like" component, we use the same generalized Navarro-Frenk-

⁷ See the definition of χ^2 in Ref. [38]

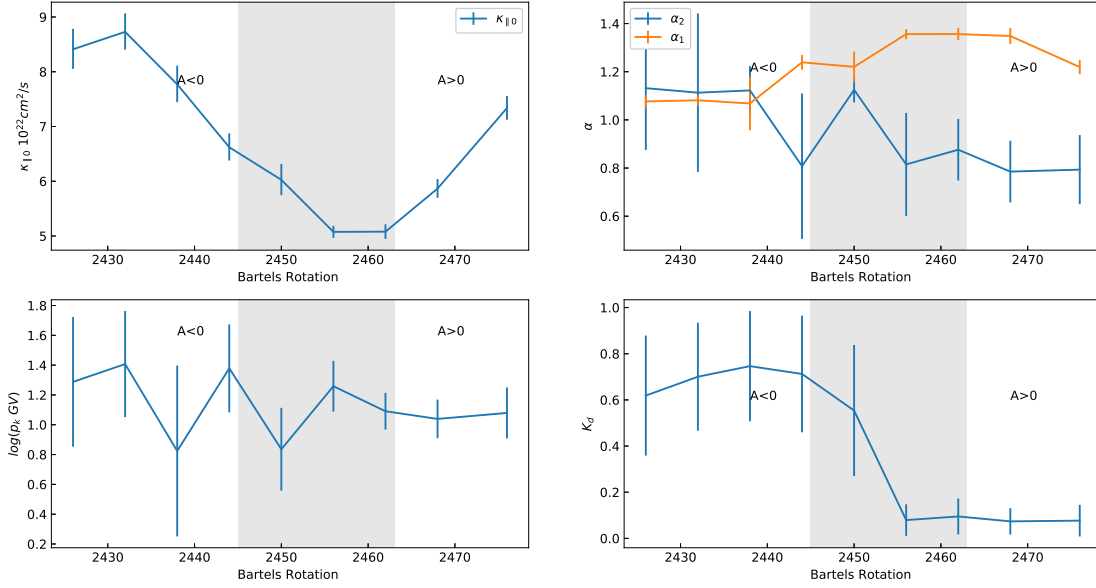


FIG. A4. The fitting solar modulation parameters and 1σ uncertainties. The period with uncertain HMF polarity is marked in gray.

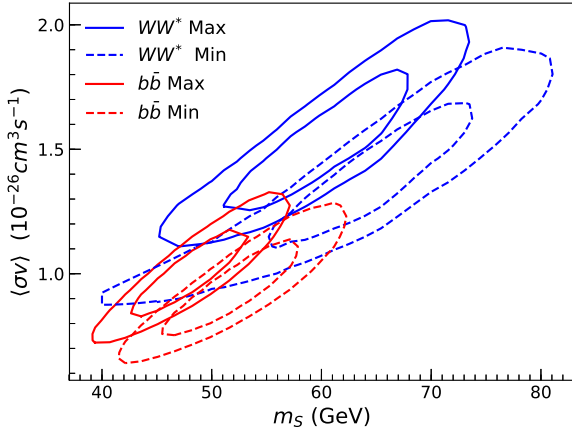


FIG. A5. The favored DM parameter regions (1σ and 2σ) by antiprotons for solar modulation parameters which enveloping the measurement uncertainties of protons.

White profile but use an independent factor to take into account the possible contribution from unresolved sources in the bulge [28, 29]. We multiply these templates with exposure maps to get the predicted photon counts. And we also use the Fermi-LAT PSF calculated by *gpsf* at the galactic center position to smooth all components to account for the finite angular resolution of the instrument.

We first choose the region satisfying $|b| < -2^\circ$ in the southern sky with less complicated structures, and fit the likelihood

with χ^2_{ext} set to zero. And we could get the estimation about the fluxes and statistical errors for the isotropic γ -ray emissions and the Fermi Bubbles, respectively. Then we choose the inner galaxy region, $|l| \leq 20^\circ$ and $2^\circ \leq |b| \leq 20^\circ$, and fit the likelihood with constraints for the isotropic γ -ray emissions and the Fermi Bubbles. The constraints are assumed to be Gaussian, as

$$\chi^2_{\text{ext}} = \sum_{i,k} \left(\frac{\phi_{i,k} - \bar{\phi}_{i,k}}{\Delta\phi_{i,k}} \right)^2 \quad (9)$$

where $\phi_{i,k}$ is the predicted flux of component k in energy bin i , $\bar{\phi}_{i,k}$ are the estimated fluxes from the $|b| < -2^\circ$ region and $\Delta\phi_{i,k}^2$ are the sum of statistical and systematic errors from the effective area, based on analysis in the $|b| < -2^\circ$ region too, in quadrature. Then we can get the scaling factor q_i for each component in each energy bin, and get the spectral energy distribution (SED) for the GCE component. To account for the systematics from the background modeling, we repeat above analysis for total 128 galactic diffuse emission templates and derive SED for the GCE component as shown in Fig. A7.

Then we scan the DM parameters ($m_S, \langle\sigma\nu\rangle$) to calculate the χ^2 map for each SED with

$$\chi^2 = \sum_i \left(\frac{\phi_i(m_S, \langle\sigma\nu\rangle) - \bar{\phi}_i}{\Delta\phi_i} \right)^2, \quad (10)$$

where $\phi_i(m_S, \langle\sigma\nu\rangle)$ is the predicted flux from the DM annihilation at the GCE region in the i th energy bin, $\bar{\phi}_i$ is the measured flux from the SED we obtained and $\Delta\phi_i^2$ is the orthogonal sum of corresponding statistical and systematic er-

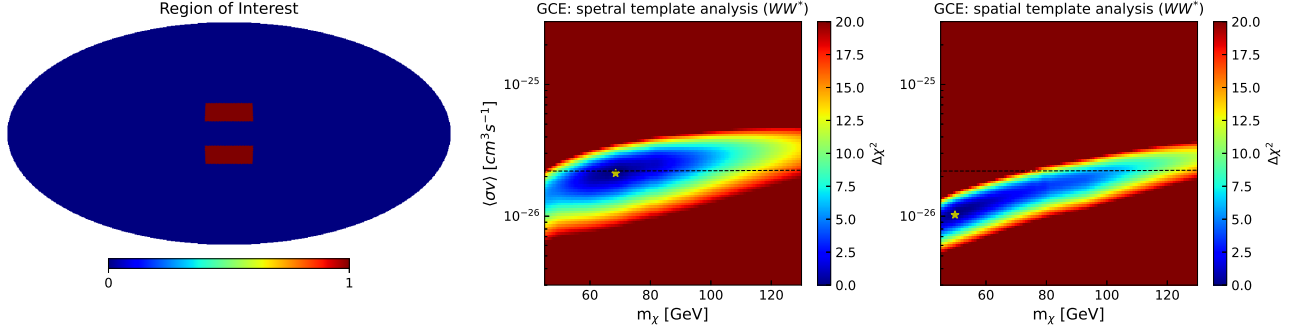


FIG. A6. Left: The ROI (brown) used in the GCE fitting. Middle: The $\Delta\chi^2$ map on the mass and cross section parameter plane for the $SS \rightarrow WW^*$ channel with the spectral template analysis. Right: The $\Delta\chi^2$ map with the spatial template analysis. The yellow stars show the best-fit DM parameters. The dashed black lines represent the mass-dependent relic annihilation cross section calculated in Ref. [57]

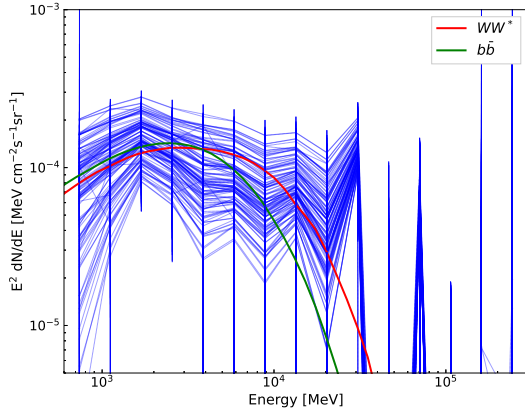


FIG. A7. The SED for the GCE component obtained from the spatial template analysis with 128 galactic diffuse emission templates. The red (green) line represents the spectrum with the best-fit DM parameters for the WW^* ($b\bar{b}$) channel.

rors from the effective area. The final result of the spatial template analysis is derived from the average of all 128 χ^2 maps. The averaged $\Delta\chi^2$ (defined as $\chi^2 - \chi^2_{\min}$) map is shown in the right panel of Fig. A6.

G. The result for the $b\bar{b}$ channel

Fig. A8 shows results from the antiproton and GCE analysis for the channel $SS \rightarrow b\bar{b}$.

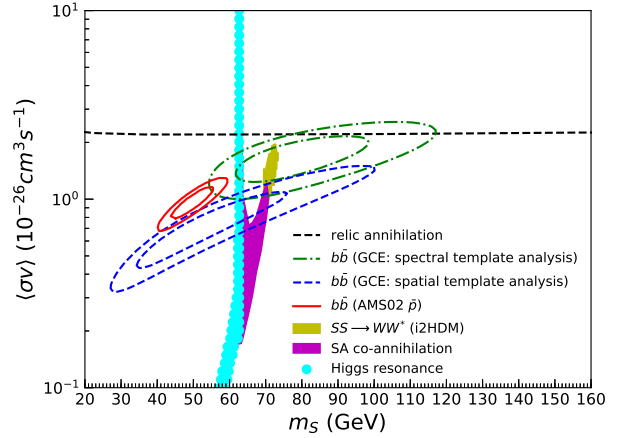


FIG. A8. The favored DM parameter space via fitting to the antiproton and GCE data (1σ and 2σ from inside to outside) for the $b\bar{b}$ channel, as well as the i2HDM model parameters to fit the W -boson mass anomaly (the 95% region, adopted from Ref. [34]). The black dashed line is the mass-dependent relic annihilation cross section [57].

-
- [1] G. Bertone, D. Hooper, and J. Silk, *Phys. Rept.* **405**, 279 (2005), hep-ph/0404175.
- [2] J. Liu, X. Chen, and X. Ji, *Nature Phys.* **13**, 212 (2017), 1709.00688.
- [3] M. Schumann, *J. Phys. G* **46**, 103003 (2019), 1903.03026.
- [4] L. Bergström and P. Ullio, *Nuclear Physics B* **504**, 27 (1997), hep-ph/9706232.
- [5] O. Adriani et al. (PAMELA), *Nature* **458**, 607 (2009), 0810.4995.
- [6] M. Aguilar et al. (AMS), *Phys. Rept.* **894**, 1 (2021).
- [7] G. Ambrosi et al. (DAMPE), *Nature* **552**, 63 (2017), 1711.10981.
- [8] I. V. Moskalenko, A. W. Strong, S. G. Mashnik, and J. F. Ormes, *Astrophys. J.* **586**, 1050 (2003), astro-ph/0210480.
- [9] D. Hooper, T. Linden, and P. Mertsch, *Journal of Cosmology and Astroparticle Physics* **2015**, 021–021 (2015), ISSN 1475-7516, URL <http://dx.doi.org/10.1088/1475-7516/2015/03/021>.
- [10] M.-Y. Cui, Q. Yuan, Y.-L. S. Tsai, and Y.-Z. Fan, *Phys. Rev. Lett.* **118**, 191101 (2017), 1610.03840.
- [11] A. Cuoco, M. Krämer, and M. Korsmeier, *Phys. Rev. Lett.* **118**, 191102 (2017), 1610.03071.
- [12] D. Hooper and L. Goodenough, *Phys. Lett. B* **697**, 412 (2011), 1010.2752.
- [13] B. Zhou, Y.-F. Liang, X. Huang, X. Li, Y.-Z. Fan, L. Feng, and J. Chang, *Phys. Rev. D* **91**, 123010 (2015), 1406.6948.
- [14] T. Daylan, D. P. Finkbeiner, D. Hooper, T. Linden, S. K. N. Portillo, N. L. Rodd, and T. R. Slatyer, *Phys. Dark Univ.* **12**, 1 (2016), 1402.6703.
- [15] F. Calore, I. Cholis, and C. Weniger, *JCAP* **03**, 038 (2015), 1409.0042.
- [16] D. Hooper, P. Blasi, and P. D. Serpico, *JCAP* **01**, 025 (2009), 0810.1527.
- [17] P.-F. Yin, Z.-H. Yu, Q. Yuan, and X.-J. Bi, *Phys. Rev. D* **88**, 023001 (2013), 1304.4128.
- [18] Q. Yuan et al. (2017), 1711.10989.
- [19] M.-Y. Cui, X. Pan, Q. Yuan, Y.-Z. Fan, and H.-S. Zong, *JCAP* **06**, 024 (2018), 1803.02163.
- [20] M.-Y. Cui, W.-C. Huang, Y.-L. S. Tsai, and Q. Yuan, *JCAP* **11**, 039 (2018), 1805.11590.
- [21] I. Cholis, T. Linden, and D. Hooper, *Phys. Rev. D* **99**, 103026 (2019), 1903.02549.
- [22] S.-J. Lin, X.-J. Bi, J. Feng, P.-F. Yin, and Z.-H. Yu, *Phys. Rev. D* **96**, 123010 (2017), 1612.04001.
- [23] H.-B. Jin, Y.-L. Wu, and Y.-F. Zhou, *Astrophys. J.* **901**, 80 (2020), 1701.02213.
- [24] J. Heisig, M. Korsmeier, and M. W. Winkler, *Phys. Rev. Res.* **2**, 043017 (2020), 2005.04237.
- [25] A. Jueid, J. Kip, R. R. de Austri, and P. Skands (2022), 2202.11546.
- [26] R. Bartels, S. Krishnamurthy, and C. Weniger, *Phys. Rev. Lett.* **116**, 051102 (2016), 1506.05104.
- [27] S. K. Lee, M. Lisanti, B. R. Safdi, T. R. Slatyer, and W. Xue, *Phys. Rev. Lett.* **116**, 051103 (2016), 1506.05124.
- [28] O. Macias, C. Gordon, R. M. Crocker, B. Coleman, D. Paterson, S. Horiuchi, and M. Pohl, *Nature Astron.* **2**, 387 (2018), 1611.06644.
- [29] R. Bartels, E. Storm, C. Weniger, and F. Calore, *Nature Astron.* **2**, 819 (2018), 1711.04778.
- [30] R. K. Leane and T. R. Slatyer, *Phys. Rev. Lett.* **123**, 241101 (2019), 1904.08430.
- [31] Y.-M. Zhong, S. D. McDermott, I. Cholis, and P. J. Fox, *Phys. Rev. Lett.* **124**, 231103 (2020), 1911.12369.
- [32] I. Cholis, Y.-M. Zhong, S. D. McDermott, and J. P. Surdutovich (2021), 2112.09706.
- [33] Aaltonen, T. et al. (CDF collaboration), *Science* **376**, 170 (2022).
- [34] Y.-Z. Fan, T.-P. Tang, Y.-L. S. Tsai, and L. Wu, *Phys. Rev. Lett.* **129**, 091802 (2022), 2204.03693.
- [35] M. S. Potgieter, E. E. Vos, R. Munini, M. Boezio, and V. Di Felice, *Astrophys. J.* **810**, 141 (2015).
- [36] X. Luo, M. S. Potgieter, V. Bindi, M. Zhang, and X. Feng, *Astrophys. J.* **878**, 6 (2019), 1909.03050.
- [37] M. Aguilar et al. (AMS), *Phys. Rev. Lett.* **121**, 051101 (2018).
- [38] X. Huang, T. Enßlin, and M. Selig, *JCAP* **04**, 030 (2016), 1511.02621.
- [39] L. J. Gleeson and W. I. Axford, *Astrophys. J.* **154**, 1011 (1968).
- [40] I. Cholis, D. Hooper, and T. Linden, *Phys. Rev. D* **93**, 043016 (2016), 1511.01507.
- [41] L. Maccione, *Phys. Rev. Lett.* **110**, 081101 (2013), 1211.6905.
- [42] M. Zhang, *The Astrophysical Journal* **513**, 409 (1999).
- [43] R. D. Strauss, M. S. Potgieter, I. Büsching, and A. Kopp, *Astrophys. J.* **735**, 83 (2011).
- [44] E. N. Parker, *Planet. Space Sci.* **13**, 9 (1965).
- [45] A. C. Cummings, E. C. Stone, B. C. Heikkilä, N. Lal, W. R. Webber, G. Jóhannesson, I. V. Moskalenko, E. Orlando, and T. A. Porter, *Astrophys. J.* **831**, 18 (2016).
- [46] Q. An et al. (DAMPE), *Sci. Adv.* **5**, eaax3793 (2019), 1909.12860.
- [47] A. W. Strong and I. V. Moskalenko, *Astrophys. J.* **509**, 212 (1998), astro-ph/9807150.
- [48] M. W. Winkler, *JCAP* **02**, 048 (2017), 1701.04866.
- [49] M. Kachelriess, I. V. Moskalenko, and S. S. Ostapchenko, *Astrophys. J.* **803**, 54 (2015), 1502.04158.
- [50] M. Aguilar et al. (AMS), *Phys. Rev. Lett.* **117**, 091103 (2016).
- [51] C.-R. Zhu, Q. Yuan, and D.-M. Wei, *Astropart. Phys.* **124**, 102495 (2021), 2007.13989.
- [52] H. Zhao, *Mon. Not. Roy. Astron. Soc.* **278**, 488 (1996), astro-ph/9509122.
- [53] J. D. Simon, *Ann. Rev. Astron. Astrophys.* **57**, 375 (2019), 1901.05465.
- [54] K. Hayashi, M. Ibe, S. Kobayashi, Y. Nakayama, and S. Shirai, *Phys. Rev. D* **103**, 023017 (2021), 2008.02529.
- [55] J. Alwall, R. Frederix, S. Frixione, V. Hirschi, F. Maltoni, O. Mattelaer, H. S. Shao, T. Stelzer, P. Torrielli, and M. Zaro, *JHEP* **07**, 079 (2014), 1405.0301.
- [56] T. Sjöstrand, S. Ask, J. R. Christiansen, R. Corke, N. Desai, P. Ilten, S. Mrenna, S. Prestel, C. O. Rasmussen, and P. Z. Skands, *Comput. Phys. Commun.* **191**, 159 (2015), 1410.3012.
- [57] G. Steigman, B. Dasgupta, and J. F. Beacom, *Phys. Rev. D* **86**, 023506 (2012), 1204.3622.
- [58] M. Selig, V. Vacca, N. Oppermann, and T. A. Enßlin, *Astron. Astrophys.* **581**, A126 (2015), 1410.4562.
- [59] W. de Boer, I. Gebauer, A. Neumann, and P. L. Biermann (2016), 1610.08926.
- [60] W. de Boer, L. Bosse, I. Gebauer, A. Neumann, and P. L. Biermann, *Phys. Rev. D* **96**, 043012 (2017), 1707.08653.
- [61] C.-T. Lu, L. Wu, Y. Wu, and B. Zhu (2022), 2204.03796.
- [62] P. Athron, A. Fowlie, C.-T. Lu, L. Wu, Y. Wu, and B. Zhu (2022), 2204.03996.
- [63] R. Abbasi et al. (IceCube), in *37th International Cosmic Ray Conference* (2021), 2107.11224.

- [64] P. L. Biermann et al., *Adv. Space Res.* **62**, 2773 (2018), 1803.10752.
- [65] P.-p. Zhang, B.-q. Qiao, Q. Yuan, S.-w. Cui, and Y.-q. Guo, *Phys. Rev. D* **105**, 023002 (2022), 2107.08280.
- [66] X. Luo, M. S. Potgieter, M. Zhang, and X. Feng, *apj* **839**, 53 (2017).
- [67] E. N. Parker, *Astrophys. J.* **128**, 664 (1958).
- [68] J. Kota and J. R. Jokipii, *Astrophys. J.* **265**, 573 (1983).
- [69] J. R. Jokipii, E. H. Levy, and W. B. Hubbard, *Astrophys. J.* **213**, 861 (1977).
- [70] R. A. Burger and M. S. Potgieter, *Astrophys. J.* **339**, 501 (1989).
- [71] M. S. Potgieter, J. A. Le Roux, and R. A. Burger, *J. Geophys. Res.* **94**, 2323 (1989).
- [72] Q. Yuan, C.-R. Zhu, X.-J. Bi, and D.-M. Wei, *Journal of Cosmology and Astroparticle Physics* **2020**, 027–027 (2020), ISSN 1475-7516, URL <http://dx.doi.org/10.1088/1475-7516/2020/11/027>.
- [73] C.-R. Zhu, Q. Yuan, and D.-M. Wei, *The Astrophysical Journal* **863**, 119 (2018), ISSN 1538-4357, URL <http://dx.doi.org/10.3847/1538-4357/aacff9>.
- [74] M. Aguilar, D. Aisa, B. Alpat, A. Alvino, G. Ambrosi, K. Andeen, L. Arruda, N. Attig, P. Azzarello, A. Bachlechner, et al., *Phys. Rev. Lett.* **114**, 171103 (2015).
- [75] X. Sun, J. T. Hoeksema, Y. Liu, and J. Zhao, *Astrophys. J.* **798**, 114 (2015), 1410.8867.
- [76] S. E. S. Ferreira and M. S. Potgieter, *The Astrophysical Journal* **603**, 744 (2004), URL <https://doi.org/10.1086/381649>.
- [77] X. Song, X. Luo, M. S. Potgieter, X. Liu, and Z. Geng, *The Astrophysical Journal Supplement Series* **257**, 48 (2021), URL <https://doi.org/10.3847/1538-4365/ac281c>.
- [78] K. M. Górski, E. Hivon, A. J. Banday, B. D. Wandelt, F. K. Hansen, M. Reinecke, and M. Bartelman, *Astrophys. J.* **622**, 759 (2005), astro-ph/0409513.
- [79] M. Ackermann et al. (Fermi-LAT), *Astrophys. J.* **750**, 3 (2012), 1202.4039.
- [80] M. Su, T. R. Slatyer, and D. P. Finkbeiner, *Astrophys. J.* **724**, 1044 (2010), 1005.5480.
- [81] S. Abdollahi et al. (Fermi-LAT), *Astrophys. J. Suppl.* **247**, 33 (2020), 1902.10045.
- [82] S. Abdollahi et al. (Fermi-LAT), *Astrophys. J. Supp.* **260**, 53 (2022), 2201.11184.